Supplementary information

Non-Integer-Dimensional Architected Materials Enabling Synergistic Acoustic, Mechanical, and Fluid Coupling

*Zichao Guo, Ziping Lei, Kexin Zeng, Yiman Chen, Zhonggang Wang *, Zheng Fan* , Zhendong Li**

Section S1. Representative non-integer dimensional configurations

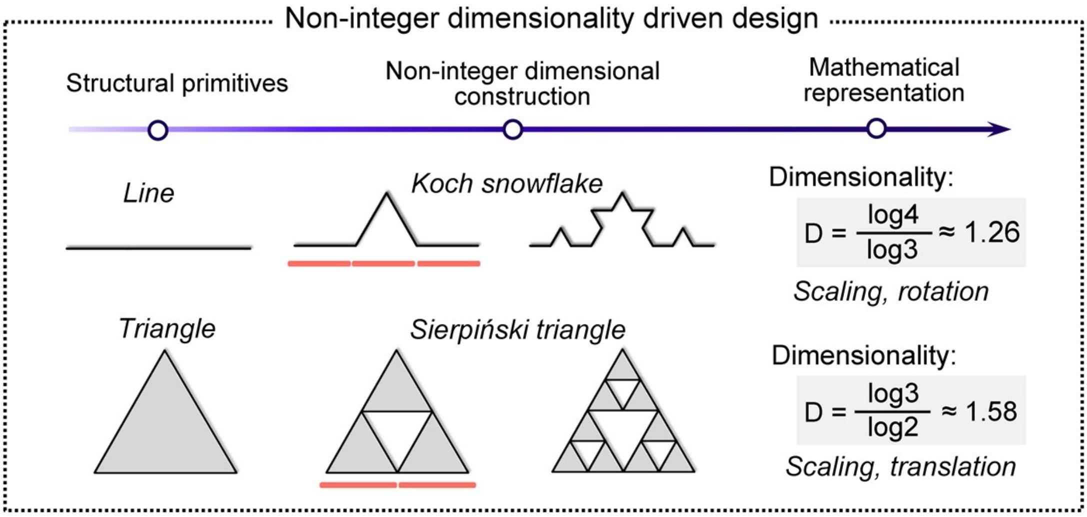

Fig. S1 Representative examples of fractal configurations (e.g., Koch snowflake, Sierpiński triangle) demonstrating self-similar and non-integer dimensional characteristic.

Section S2. Fabrication of fractal architectures

The proposed fractal architectures were fabricated using digital light processing (DLP) 3D printing, a technique known for its high precision and efficiency in producing fine-featured components, as illustrated in Fig. 2(C). A commercially available standard photopolymer resin (Nova 3D, China) was used as the printing material. Upon completion of printing, the specimens were thoroughly rinsed in isopropyl alcohol (IPA) for approximately 20 minutes to remove any residual uncured resin, followed by drying with a high-power air blower. Subsequently, the samples were post-cured in an ultraviolet (UV) chamber for 30 minutes under 405 nm LED light to ensure complete polymerization and mechanical stabilization.

Section S3. Sound transmission loss of first- to third-order NDAMs

To highlight the sound insulation performance of the proposed design, the sound transmission loss (STL) of the first- to third-order NDAMs is shown in Fig. S2. And the STL was evaluated using the ratio of acoustic energy flux:

$$STL = 10\log_{10}\frac{W_{in}}{W_{out}} \tag{S1}$$

where W_{in} and W_{out} denote the incident and transmitted acoustic power, respectively, computed from the surface integrals of acoustic intensity. The acoustic field was modeled using the Pressure Acoustics and Thermoviscous Acoustics modules. The solid–air interfaces were treated as rigid boundaries, and thermoviscous losses associated with boundary-layer effects in the narrow multiscale channels were included to capture realistic sound transmission and attenuation. The regions of high sound insulation align with the band gap positions in Figure. 3A of the main text (from Γ to X direction), and all three structures demonstrate excellent sound insulation capabilities.

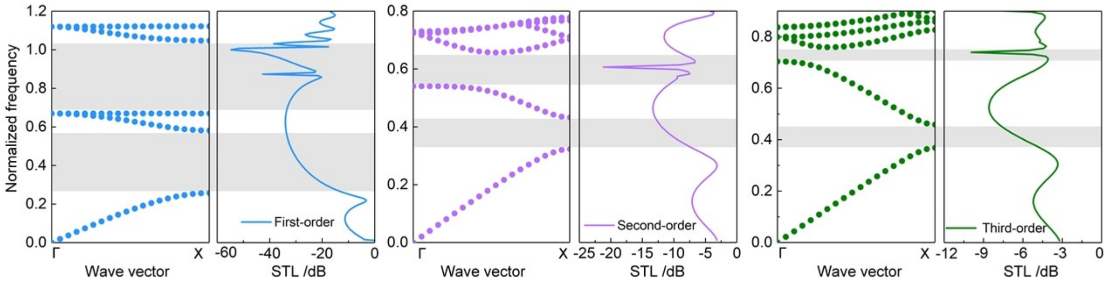

Fig. S2 Sound transmission loss of first- to third-order NDAM under normal incidence of sound waves (from Γ to X direction).

The sound-insulation properties of first- to third-order NDAMs aligned in series were analyzed, with the periodic unit comprising solid and air phases, as illustrated in Fig. S3(A). The corresponding STL is presented in Fig. S3(B), demonstrating effective sound insulation across a broad frequency range, from low to ultrahigh frequencies. Additionally, the sound pressure distributions for the structure at representative frequencies are depicted in Fig. S3(C). In the corners and sharp edges of fractal geometries, sound waves become locally concentrated, leading to significant enhancements in local sound pressure [S1]. As the frequency increases, the region of sound energy dissipation gradually shifts toward higher-order NDAMs. This progressive transition from low to high frequencies ensures that the structure's sound insulation performance effectively spans a broad spectrum, from low to ultrahigh frequencies, offering superior soundproofing capabilities compared to a single NDAM.

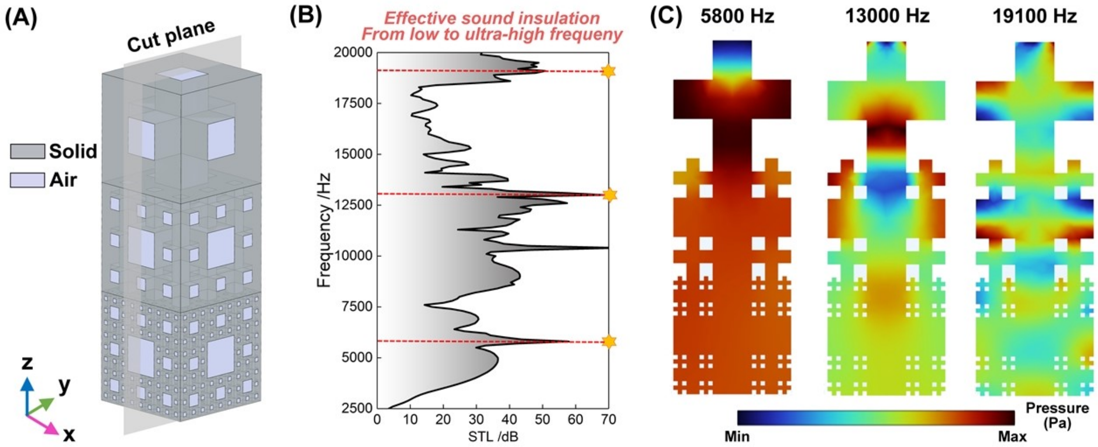

Fig. S3 (A) Periodic unit comprising solid and air phases. (B) Sound Insulation property of corresponding structure. (C) Sound pressure distributions with typical frequencies of 5800 Hz, 13000 Hz, and 19100 Hz, respectively.

Section S4. Elastic modulus of NDAMs

The elastic modulus distribution of NDAMs is derived from stiffness matrices, as detailed in reference S2. These stiffness matrices were computed using the Micromechanics Plugin in the finite element analysis software ABAQUS. This plugin performs micromechanical analysis to calculate the effective macroscopic stiffness matrices of composite materials or porous structures based on the stress-strain response of individual elements. This method effectively captures the anisotropic elastic properties of complex geometries, making it particularly suitable for Menger sponge structures. The Zener anisotropy index is a quantitative measure used to assess the elastic anisotropy and is defined as:

$$A=\frac{2C_{44}}{C_{11}-C_{12}}\#(S2)$$

where C_{11}, C_{12}, and C_{44} are the elastic constants of the material (independent components of the elastic stiffness matrix).

Section S5. Crushing process of NDAMs

The quasi-static crushing process of NDAMs is illustrated in Fig. S4. At a strain of $\varepsilon = 0.02$, the structures remain in the elastic stage, with overall deformation being uniform and no apparent local failure observed. As the strain increases to $\varepsilon = 0.08$, the structures transition into the plastic deformation stage, where noticeable deformation appears in the pore regions across all orders. When the strain further increases to

$\varepsilon = 0.15$, local failure occurs in all NDAMs. In the first-order NDAM, failure concentrates at the pore corners where stress is most intense. With increasing hierarchical order, the failure mechanism of the NDAMs transitions from localized failure to more uniform damage. The third-order NDAM exhibits a significant coupling effect of compression and shear failure.

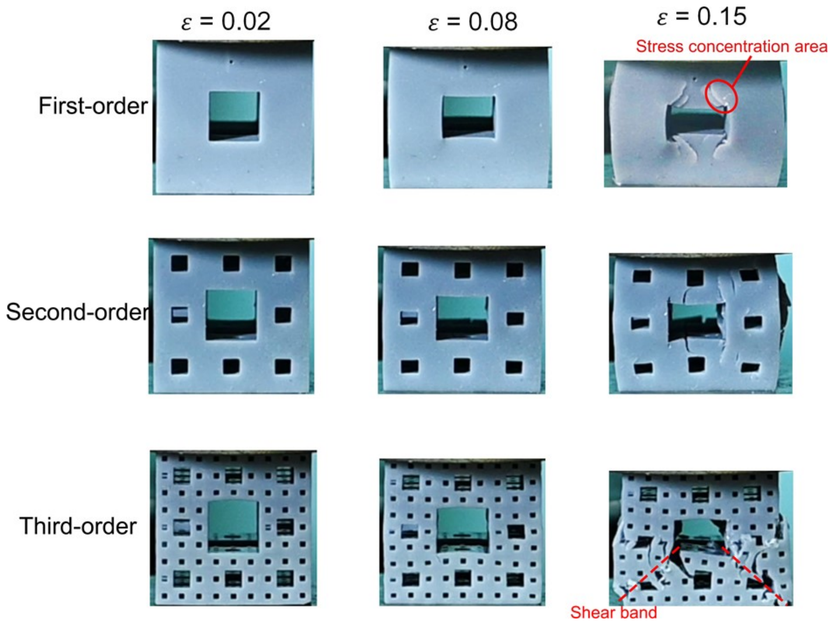

Fig. S4 The quasi-static crushing process of first- to third-order NDAMs.

Section S6. Impact resistance metrics of NDAMs

The key crashworthiness metrics $^{S2\text{-}S6}$ of NDAMs are presented in Table S1. The first-order NDAM exhibits an elastic modulus E of 551.79 MPa and a mean crushing force (MCF) of 8120.90 N, indicating its high structural stiffness and load-bearing capacity. Additionally, it achieves the highest specific energy absorption (SEA) of 1.68 J/g, suggesting that it can absorb more impact energy per unit mass. However, its peak force (PF) reaches 14049.15 N, indicating that it may generate significant impact loads during actual collisions, which could be detrimental to the protected objects. The second-order NDAM demonstrates the highest crushing force efficiency (CFE) of 0.73 while maintaining a relatively high SEA of 1.22 J/g, reflecting a well-balanced performance between energy absorption and impact load mitigation. The third-order NDAM, with the lowest peak force of only 4483.76 N, achieves a CFE of 0.68, indicating remarkable buffering and protective performance despite its relatively lower load-bearing capacity. Overall, as the order of the NDAM increases, its geometric structure evolves from simple, regular single cells to complex, multi-level fractal features. This geometric evolution significantly influences its mechanical properties and functional orientation.

Table S1. Key crashworthiness metrics of NDAMs.

NDAMs	E(MPa)	SEA(J/g)	MCF(N)	CFE	PF(N)
First-order	551.79	1.68	8120.90	0.58	14049.15
Second-order	310.77	1.22	5423.23	0.73	7429.83
Third-order	172.50	0.85	3029.57	0.68	4483.76

Section S7. Air pressure distributions of NDAMs

The air pressure distributions of first- to third-order NDAMs are illustrated in Fig. S5. Upstream of the structure, the airflow retains a higher pressure; however, as it passes through the geometry, it forms localized low-pressure regions around the structure. With increasing airflow velocity, a negative-pressure region develops downstream of the structure, consistent with the flow-velocity distribution^{S7}. As the fractal order increases, the pressure gradient becomes more uniform. The self-similar configuration of the fractal structure minimizes pressure fluctuations in fluid impact regions, prevents localized pressure concentrations caused by single-scale features, and facilitates smoother flow, thereby significantly enhancing flow efficiency.

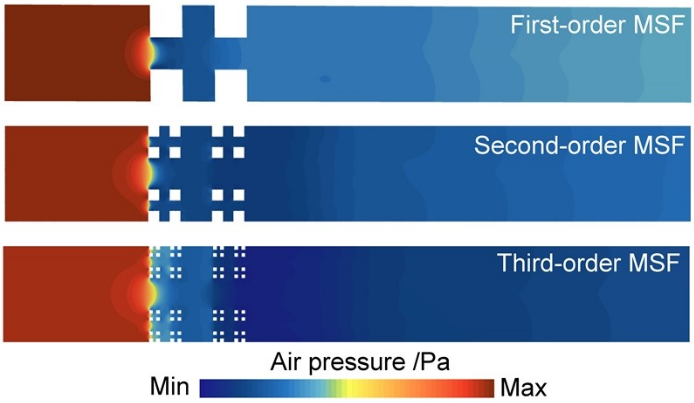

Fig. S5 Air pressure distributions of first- to third-order NDAM.

Section S8. Air drags with different inlet velocities of NDAMs

The air drag of first- to third-order NDAMs was further compared under different inlet wind velocities. As shown in Fig. S6, the air drag decreases with increasing fractal order across different inlet velocities, and this reduction trend becomes more pronounced at higher flow speeds. This result demonstrates that the multi-scale configuration of fractal structures effectively distributes fluid drag across multiple scales, significantly reducing aerodynamic drag.

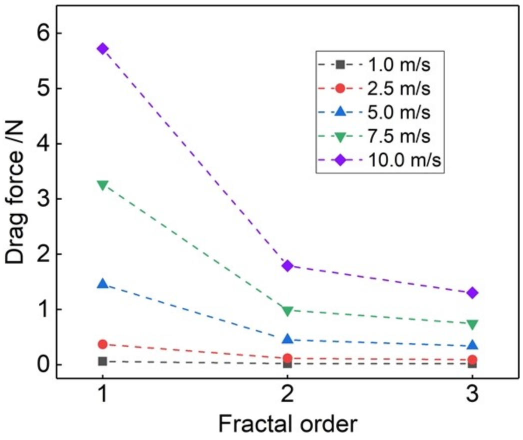

Fig. S6 Air drag of first- to third-order NDAM with different inlet air velocity.

Section S9. Topological designs with varying fractal dimensions

The NDAM is constructed based on the recursive central-region removal method, in which the initial cube is first equally divided into smaller units according to a scaling factor $1/\varepsilon$, and then a specific number $N(\varepsilon)$ of sub-cubes are retained based on predefined rules [S8], while the remaining parts were removed. Herein, three cases of different fractal dimensions were selected for investigation: D = 2.73 ($N(\varepsilon)$ = 20, $1/\varepsilon$ = 3), D = 2.5 ($N(\varepsilon)$ = 32, $1/\varepsilon$ = 4) and D = 2.35 ($N(\varepsilon)$ = 44, $1/\varepsilon$ = 5), as shown in Fig. S7. For each dimension, the equal-division and preservation operations were iteratively repeated starting from the initial cube, and the number of iterations defined the fractal order. First-, second-, and third-order NDAMs were generated for each fractal dimension, resulting in a total of nine different configurations, to systematically investigate the correlation between fractal geometric properties and multiphysics field performance.

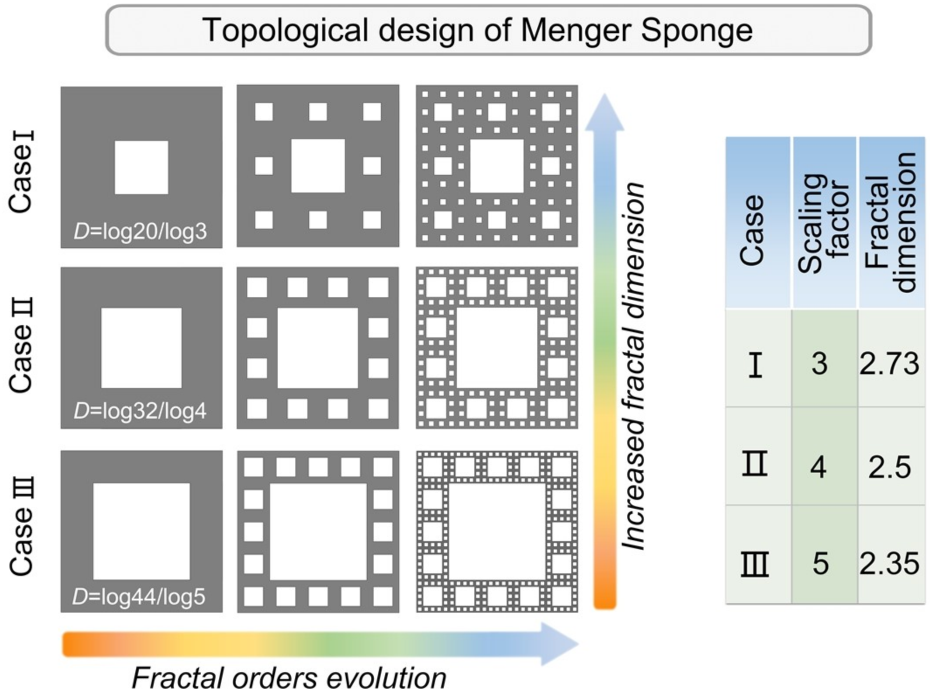

Case	Scaling factor	Fractal dimension
I	3	2.73
II	4	2.5
III	5	2.35

Fig. S7 Topological design of NDAMs with varying fractal dimensions. Evolution of NDAMs and fractal dimensions with 2.73 to 2.35.

Fig. S8(A) presents a comparative analysis of the average STL of NDAMs over a frequency range of 10 kHz. A significant observation is that a decrease in fractal dimension leads to a decline in STL. This is primarily due to the increased voids in the structure, allowing more sound to be transmitted. Additionally, smaller pore resonance frequencies shift higher, further reducing the average STL across the simulated frequency range. Fig. S8(B) presents a comparative analysis of air drag and the corresponding front surface porosity, demonstrating a significant improvement in ventilation efficiency. Fig. S8(C) illustrates the normalized evolutionary trends of the key mechanical properties of NDAMs as a function of fractal dimension and order. Overall, as the fractal dimension decreases and the fractal order increases, the structural performance transitions from high stiffness and strength to greater flexibility due to increased porosity and the expansion of stress transmission pathways. Specifically, NDAMs with high dimensionality and low fractal order exhibit the highest elastic modulus and SEA, indicating superior load-bearing capacity and energy absorption performance. However, their high peak impact force during collisions may limit their applicability in impact-sensitive protective scenarios. In contrast, NDAMs with intermediate dimensionality and low fractal order achieve the optimal CFE, signifying a well-balanced trade-off between impact mitigation and energy absorption, making them a well-rounded structural design with superior overall performance. Notably, NDAMs with low dimensionality and high fractal order do not exhibit superior CFE. This can be attributed to their excessively high porosity, which renders them prone to local buckling under compression, leading to a reduction in plateau stress and compromising their stable energy absorption capacity.

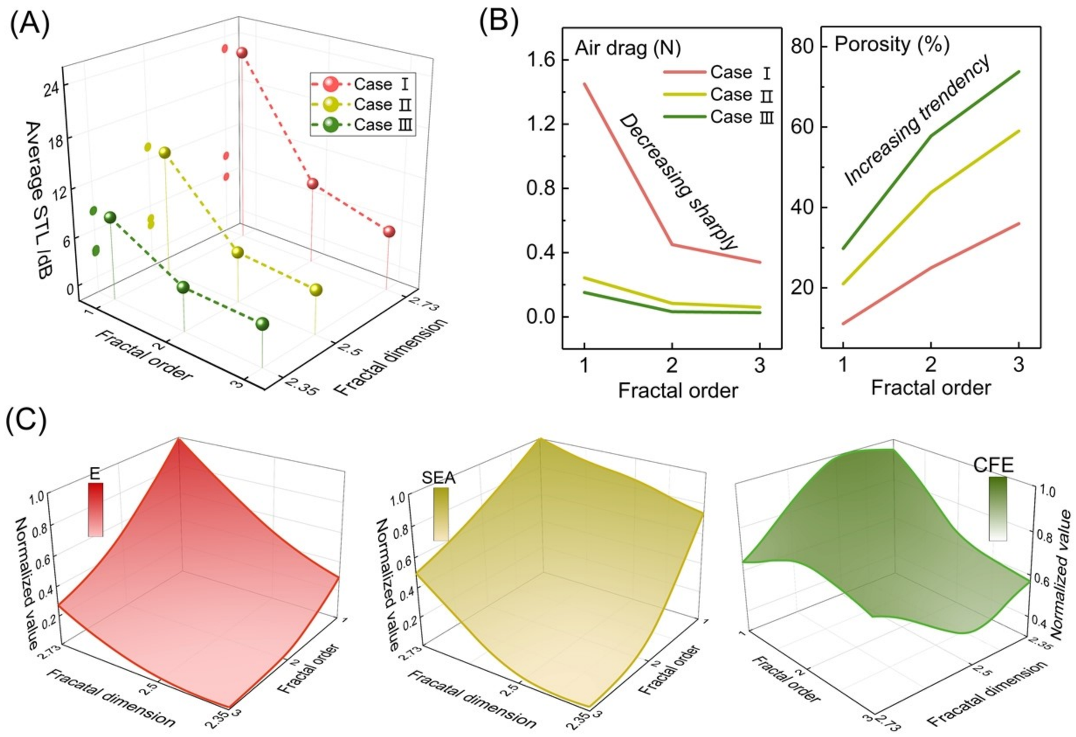

Fig. S8 Multifunctional performance of corresponding topological design (A) Comparative analysis of average STL with the frequency range of 10 kHz. (B) Comparative analysis of air drags and front surface porosity along with different NDAMs. (C) Evolutionary trends of the key mechanical properties of NDAMs as a function of fractal dimension and order.

Section S10. Summary of superior mechanical and acoustic metamaterials.

Table. S2 compares the proposed non-integer dimensional strategy with representative state-of-the-art metamaterial designs. Each configuration is evaluated based on key performance metrics, with scoring conducted as objectively and consistently as possible.

Table S2. Comparison with prevailing advanced metamaterials.

	This work	Lattice	Honeycomb	Advanced porous materials	Topology optimized structure

Intrinsic multifunctionality	Achieves full integration of acoustic, mechanical, and fluid functions without hybrid modules. (7/7)	Enables basic multifunctionality, but lacks seamless integration across physics domains. (6/7)	Provides structural and mechanical functionality; limited inherent multifunctionality. (3/7)	Tunable porosity enables filtering, damping, or insulation; limited structural control. (4/7)	Multi-objective optimization enables hybrid function; coupling constrained by design space. (6/7)
Sound insulation	Multiband attenuation via hierarchical resonance and scattering. (6.5/7)	Moderate acoustic isolation due to periodicity, yet lacks tunability or broadband response. (6/7)	Regular pattern contributes little to sound isolation without added materials or components. (3/7)	Tunable pore size support effective sound attenuation over moderate frequency ranges. (7/7)	Strong low-frequency performance via resonant cavities; adaptability is limited. (6/7)
Mechanical energy absorption	Hierarchical topology promotes distributed deformation and energy dissipation. (6/7)	Excellent impact mitigation enabled by tailored cell topology and deformation modes. (5/7)	Superior crash energy absorption from axis-aligned buckling and in-plane deformation. (6.5/7)	Energy dissipation often limited by irregular pore shape and low structural stiffness. (3/7)	Topology optimization can concentrate material for effective impact dispersion. (6/7)
Ventilation / thermal dissipation	Improves airflow and heat transfer through interconnected pores and fractal channels. (6.5/7)	Partially open channels allow moderate airflow. (6/7)	Airflow possible if unsealed; otherwise, negligible in functional settings. (5/7)	Microchannels allow air permeation, but with high resistance. (6.5/7)	Limited internal channel connectivity hinders airflow efficiency. (4/7)
Fabrication feasibility	Printable via DLP with acceptable resolution; fabrication scalability may improve with technology. (6.5/7)	Manufacturable using photopolymer or metal printing; geometries are repetitive and modular. (6/7)	Scalable and widely manufacturable using low-cost industrial methods. (7/7)	Foam-based or layered materials are broadly scalable; some designs may need high precision. (5/7)	3D-printable in small scales; complexity increases cost and printing resolution requirements. (5.5/7)

Reference

[S1] X. Li, M. Zhao, X. Yu, J. W. Chua, Y. Yang, K. M. Lim, and W. Zhai, *Mater. Des.* 2023, **234**, 112354.

[S2] Z. Wang, Z. Lei, Z. Li, K. Yuan, and X. Wang, *Thin-Walled Struct.* 2021, **167**, 108235.

[S3] H. Yin, W. Zhang, L. Zhu, F. Meng, J. Liu, and G. Wen, *Compos. Struct*. 2023, **304**, 1–40.

[S4] V. Rai, H. Ghasemnejad, J. Watson, J. Gonzalez-Domingo, and P. Webb, *Eng. Struct.* 2019, **199**, 109620.

[S5] Z. Li, X. Liu, C. Wang, Y. Zhang, J. Qian, C. Zhang, and J. Li, *Adv. Funct. Mater.* 2024, **34**, 2420207.

[S6] M. Bogahawaththa, D. Mohotti, P. Hazell, H. Wang, K. Wijesooriya, and C. Lee, *Thin-Walled Struct.* 2025, **206**, 112704.

[S7] P. Raphe, H. Fellouah, S. Poncet, and M. Ameur, *Build. Environ.* 2021, **204**, 108118.

[S8] M. Zhao, H. Qing, Y. Wang, J. Liang, M. Zhao, Y. Geng, J. Liang, and B. Lu, *Mater. Design.* 2021, **200**, 109448.